Arabian Journal of Chemistry (2022) **15**, 103733

King Saud University

Arabian Journal of Chemistry

www.ksu.edu.sa
www.sciencedirect.com

ORIGINAL ARTICLE

A collagen(Col)/nano-hydroxyapatite (nHA) biological composite bone scaffold with double multi-level interface reinforcement

Tierong Bian [a], **Hongyun Xing** [b,*]

[a] *Medical Experimental Center, The Affiliated Hospital of Southwest Medical University, Luzhou 646000, China*
[b] *Hematology Department, The Affiliated Hospital of Southwest Medical University, Luzhou 646000, China*

Received 20 October 2021; accepted 23 January 2022
Available online 1 February 2022

KEYWORDS

Bionic bone structure;
Biomineralization;
Mineralization nucleation mechanism;
nHA array;
The double multiscales strengthening mechanism

Abstract *Introduction:* Bone scaffold is expected to possess excellent mechanical and biological properties similar to natural bone tissues. In this study, we aimed to prepare a biomineralized Col and hydroxyapatite composite scaffold consisting of biomimetic bone components and multi-level bionic bone structure to strengthen its mechanical properties.

Methods: We prepared a Col/nano-hydroxyapatite biological composite scaffold with multi-level structure (from nanofibers to micron bionic bone motif to bionc bone scaffold) of biomimetic bone tissue, and biomineralized the scaffold in simulated body fluid (SBF) preheated to 37 °C. X-ray diffraction (XRD), Fourier transform infrared (FTIR) spectroscopy and Scanning electron microscope, were used to characterize the biomineralized products.

Results: Morphological study confirmed *in situ* deposition of nHA in the multi-scale hierarchical structure of the biomineralized scaffold. We explored the biomineralization nucleation mechanism of the scaffolds at the atomic level based on the first principles and the mechanisms for growth of mineralized nHA crystal array in its multi-scale structure, and how the double multiscales structure strengthened the mechanical properties of the material.

Conclusions: This synthetic bone scaffold, with bionic bone composition and double multi-level interface reinforcement, provides a new strategy for synthesizing bioactive bone scaffolds with enhanced biomechanical properties.

1. Introduction

Bone defect repair relies heavily on the use of various bone graft materials (Zhu et al., 2020; Chen et al., 2019; Sugandha et al., 2019; Pereira and Habibovic, 2018; Yi et al., 2017; Kesireddy and Kasper, 2016; Wang et al., 2014; Cheng et al., 2014). Each year, more than 4 million surgeries are performed

* Corresponding author.
E-mail address: xinghy52003@163.com (H. Xing).
Peer review under responsibility of King Saud University.

Production and hosting by Elsevier

https://doi.org/10.1016/j.arabjc.2022.103733
1878-5352

globally for treatment of bone defects using bone grafts or bone replacement materials (Turnbull et al., 2018; Zhang et al., 2018). Currently various materials are used for bone defect repair, including autografts, allografts, xenografts and synthetic grafts, but these materials are associated with relatively high incidences of pain, infections and donor site morbidity (Walsh et al., 2018; Dorozhkin, 2009; Navarro et al., 2008; Seal et al., 2001; Lakshmi and Cato, 2006; Zimmermann and Moghaddam, 2011). An artificial bone scaffold with excellent performance resembling an autogenous bone is therefore highly desirable.

In recent years, the development of nanotissue engineering has enriched the understanding of the fundamental structures of tissues at the molecular and even the atomic levels and how these structures facilitate the execution of specific tissue functions. The emergence of bionic nanomaterials with specific functions makes it possible to better repair, preserve or improve the function of damaged tissues, and provides strong technical support for tissue engineering research (Zheng and Guo, 2004; Zheng and Guo, 2003; Guo and Zheng, 2004; Guo et al., 2002). Studies (Fatemeh et al., 2015) have shown great potentials of composite scaffolds based on natural biomaterials in reconstruction of bone defects.

Natural Col, as the major protein component in bone tissues, has excellent biocompatibility, high biodegradability, low antigenicity, and good hemostatic and cell-binding properties. Col is also deemed as one of the most important natural materials for delivery of growth factors in bone tissue engineering (Mehdi et al., 2016). These excellent properties make Col a promising candidate of bone scaffold material for bone defect repair. But Col has poor mechanical strength and is not suitable for use without modification in bone tissue engineering. So far numerous studies have shown that appropriate modification of Col can improve the mechanical properties of Col-based composite scaffolds (Shirin et al., 2019; Türk et al., 2018; Shirin et al., 2016; Sara et al., 2010).

Hydroxyapatite (HA) is an important bioactive material for bone tissue engineering. HA bears many chemical and structural similarities to natural bones, and has been shown to promote bone tissue regeneration and form chemical bonds with host bone tissues to achieve complete integration to the local bone tissues through calcium and phosphorus ion exchanges (Scarano et al., 2003). As a bone graft material, HA is also noted for its good biocompatibility, low toxicity, low risk of carcinogenicity, and the absence of fibrous tissue growth at the interface between HA implants and the regenerated bone tissue (Unnithan et al., 2015). Moreover, HA has the potential as a carrier for delivering some growth factors such as bone morphogenetic proteins to promote bone regeneration. The incorporation of HA into a Col matrix as a bone scaffold is expected to achieve similar bioactivity and osteoconductivity of a living bone (Shuai et al., 2021).

For an artificial bone scaffold, simulation of merely the bone composition is not sufficient to ensure its good biological and mechanical properties resembling natural bone tissues, whose excellent mechanical properties are also attributed to their multi-layer structures resulting from natural adaptation (Mayya et al., 2016). Mimicking the hierarchical structure of natural bone tissues has proved to enhance the mechanical strength of a scaffold material. Nevertheless, fabricating a bone scaffold with hierarchical structure can be technically challenging (Salgado et al., 2016); so far no bottom-up biological scaffold has yet been successful to faithfully reproduce the complex structure of natural bones, whose excellent load-bearing capacity is closely associated with their structural architecture and mineralization of the Col fibrils (Li et al., 2017; Xie et al., 2019). In addition, optimization of the building block components and enhancing the interfacial bonding are also critical to improve the mechanical properties of a synthetic bone scaffold (Mao et al., 2016). Synthetic nacre produced through a approach simulating the process of natural mineralization, known as the "assembly and mineralization", has been shown to possess similar mechanical properties to natural shells (Reznikov et al., 2016), and the biomineralization technique has inspired innovative approaches to the design and synthesis of composite materials for bone tissue repair (Tang et al., 2021; Gkioni et al., 2010). In biomineralized bone-like products, nano hydroxyapatite (nHA) is the key regulator that determines the bonding of the scaffold material to natural bone tissues (Deng et al., 2016; Hyeryeon et al., 2016; Huang et al., 2011), and excellent attachment strength between the scaffold and the bone tissue can be achieved when efficient *in situ* mineralization occurs in the scaffold (Yu et al., 2017; Pei et al., 2019). The highly ordered structure of a biomineralized product helps to avoid the aggregation of low-dimensional nanomaterials; which restricts their use as reinforcements in polymers (Shuai et al., 2019; Meyers et al., 2008). Such structures also confer sufficient strength and fracture toughness on the bone scaffolds to enhance their mechanical properties (Wilcock et al., 2017; Bian et al., 2019).

In this study, we prepared a Col/nano-hydroxyapatite biological composite scaffold with multi-level structure (from nanofibers to micron bionic bone motif and then to bionic bone scaffold) of biomimetic bone tissue, and biomineralized the composite scaffold in SBF preheated to 37 °C. We explored the mechanism of *in situ* nucleation of the biomineralization products by simulated computation using the first principles, investigated the growth patterns of the mineralized crystal array, and examined the possible mechanisms for enhancing the mechanical properties of biomineralized scaffold.

2. Experiment

2.1. Materials

All the reagents listed below were of analytical grade (AR), and were used directly without any further purification: nano-HA powder (20–50 nm in diameter; Nanjing Epui Nanometer Material Co. Ltd, China), PVP (relative molecular mass 1 300 000; Aladdin Industrial Co., China), type I Col (Sichuan Ming Let Biotechnology Co., LTD., China), hexafluoroisopropanol (HFIP; Chengdu Aike Chemical Reagent Co., LTD, China), and glutaraldehyde (Chengdu Aike Chemical Reagent Co., LTD, China).

2.2. Construction of the composite scaffold with biomimetic multi-scale hierarchical bone structure

The biomimetic scaffold with a multi-scale hierarchical structure was fabricated following the protocols in our previous work (Türk et al., 2018). Briefly, PVP (1.18 g) was dissolved in 10 ml absolute ethyl alcohol to prepare the sol-gel solution. HA nanoparticles (1.18 g) were then added into 10 ml absolute

ethyl alcohol and sonicated for 30 min twice to prepare the HA suspension, which was subsequently mixed with PVP sol-gel solution. The mixture was votexed using a magnetic stirring apparatus and sonicated for 30 min twice to obtain stable and homogeneous spinning solution. The solutions were then spun using with an electrospinning apparatus, with a rolling cylinder as the collector (rotation speed of 2700 rpm). The setting of the electrospinning parameters set was as the following: voltage of 20 kV, flow rate of 0.05 ml h^{-1}, and receiver distance of 12.5 cm. The orderly Col/nHA composite nanofibers were prepared by sintering the PVP/nHA composite fibers, followed by impregnation with Col solution.

The multi-layer structure of natural bone tissues is composed mainly of the hierarchical Haversian bone motifs. The lamellar structure of the bone motifs is formed by the thin, pliable Col fiber membrane, deposited layer upon layer with HA. The bionic Haversian bone motifs (500 μm in diameter) were assembled by layer-by-layer coiling into a composite membrane of biomimetic bone consisting of orderly aligned Col/nHA composite nanofibers. The bonding between the layers was achieved by filling Col between the membrane layers. Finally, according to the macroscopic structure of human compact bone, the biomimetic bone motifs were orderly aligned in close adherence to each other using Col to construct the multi-level bioinspired bone scaffold.

2.3. Biomimetic mineralization of the scaffolds

To simulate the *in vivo* mineralization conditions, we prepared simulated body fluids (SBF) following the protocols in previous descriptions (Keaveny et al., 2001). Briefly, chemical reagents completely dissolved in 700 ml deionized water (DI-H_2O) and magnetically stirred at 37 °C to prepare the 10 × SBF stock solution. The final pH of the stock solution was adjusted to 6.5 by addition of 1.0 M HCl and TRIS (to prevent precipitation) to a final volume of 1000 ml. The stock solution was stored at 4 °C. The scaffold was immersed in 10 × SBF preheated to 37 °C, vortexed gently for 6 h, carefully rinsed with phosphate buffers (PBS) for 3 times (5 min each time), and dried at 37 °C in an oven to obtain the biomineralized scaffolds.

2.4. Characterization of the scaffolds

The microarchitecture of the scaffold was scanned using micro-computed tomography (micro-CT; Siemens Inveon 3125, USA). X-ray powder diffraction (XRD) patterns of the scaffolds were obtained (Rigaku D/Max 60 kV, Cu Kα radiation, λ = 1.5406 Å). FTIR spectra was recorded on a Shimadzu Pretige-21 FTIR spectrometer. The measurements were performed on films containing KBr and the samples. Scanning electron microscopic (SEM) images of the scaffolds before and after immersion in SBF were acquired using a JEOL JSM-6700F microscope. Pt conductive coating of the scaffolds was performed before SEM measurements. The mechanical properties of the scaffolds were tested using a high-temperature electronic testing machine at the compression speed of 1 mm/min, with a loading force perpendicular to the long axis and parallel to the axial direction of the fibers of the scaffold. We prepared the scaffolds into φ6 mm × 12 mm specimens according to the standard specimen size range for compression test recommended by Keaveny et al. (Lievers et al., 2010; Lievers et al., 2010; Sigel and Martin, 1982).

2.5. Mechanism of biomineralization nucleation of the scaffold

In the study, we attempted to enhance the mechanical and biological properties of the scaffolds by mineralization, which may provide a more favorable microenvironment for bone regeneration. Helmut et al (Smith et al., 2015; Norwitz et al., 1986) believed that the mechanical performance of the Col matrix was determined by the position of mineralization, but provided no specifications concerning the sites of mineralization nucleation, binding energy during mineralization, and the optimal structure of Col for calcium ion binding at the molecular and/or atomic level. The first-principle calculation, using a simplified structure model of the material, can simulate the influences of various properties of a given material on the reaction between the materials and reveal the mechanism of such a reaction at the atomic and molecular levels. In the case of Col, its basic structural unit is a three-stranded helix (Cui et al., 2009; Persikov et al., 2005) with a primary structure characterized by the repetition of the glyine-proline-hydroxyproline (-gly-pro-hyp-) polypeptide sequence. On the basis of such structural characteristics, we constructed a simplified Col model. By the first-principle and quantum chemical calculation of the density functional theory (DFT) (Takahashi et al., 2001; Dieguez et al., 2005; Dieguez et al., 2004; Lai et al., 2005; Meyer and Vanderbilt, 2001; Lee et al., 2007; Matsunaga, 2008; He et al., 2017), considering the electrostatic potential, polarity, stereochemistry, space symmetry and surface morphology, we used B3LYP/ 6-31G* group for analogous calculations of the mineralization nucleation sites, binding energy during mineralization, and the optimal structure of the carboxyl group and/or the carbonyl group in Col bound with Ca^{2+} at the atomic level. The electron cloud distribution perspective and the electrostatic potential diagram of the atomic structure were used to predict the molecular behaviors (Cui et al., 2009) to reveal the mechanism of mineralization nucleation and the pattern of *in situ* growth of nHA arrays in the scaffold.

3. Results and discussion

3.1. Biomimetic mineralization analysis of the scaffolds

Fig. 1 presents the results of SEM showing the morphology of the scaffold after bionic mineralization. The biomineralization products on the scaffold were evenly distributed in the space between bionic bone motifs (indicated by the red arrow in Fig. 1a) and between the fibrous membrane (Fig. 1d, e), on the nanofiber membrane (arrow in Fig. 1b), and in the nanofibers (red arrow in Fig. 1e, f). Fig. 1a, b show the cross-sectional scanning images of the mineralized scaffold, and Fig. 1d-f show its longitudinal scanning images. At a greater magnification, the mineralized products appeared as elliptic clusters formed by self-assembled nanoscale flakes (Fig. 1c), and were uniformly deposited between the layers of the nanofiber membranes (Fig. 1b, d) and bonded to the bionic bone motifs. These findings confirmed the homogeneous deposition

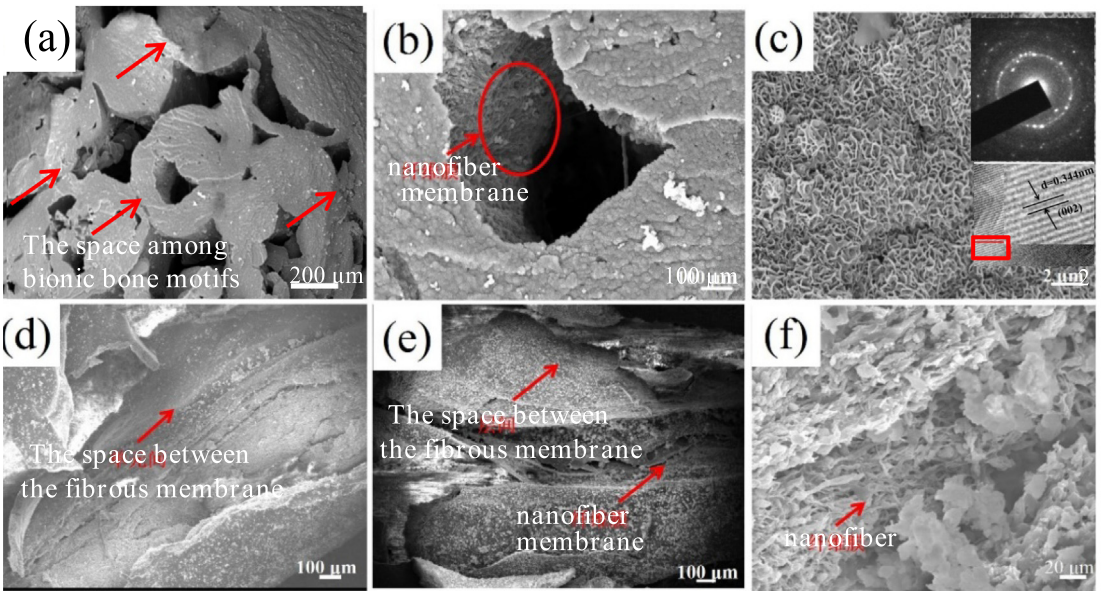

Fig. 1 SEM morphology of biomineralization products deposite on macro-micro structures of bionic scaffold (a- Biomineralized scaffolds and the space among bionic bone motif; b- Bionic bone motif; c- Biomineralization products SEM morphology, diffraction pattern of TEM, HRTEM and SAED; d, e- Between nanofiber membrane layers and on nanofiber membrane; f-Nanofibers).

of the self-assembled mineralization product at all structural levels of the scaffolds to achieve efficient mineral deposition.

3.2. XRD and FTIR characteristics of the biomineralized products

Fig.2A shows the XRD pattern of HA powder (Fig. 2A-a), Col (Fig. 2A-b) and the unbiomineralized and biomineralized Col/HA composite scaffold (Fig. 2A-c, d). The Col/HA composite scaffold biomineralized for 6 h showed a strong peak of HA (Fig. 2A-d), resulting mostly from the biomineralized product HA rather than HA component in the nanofiber.

Fig. 2B shows the FTIR spectra of HA powder (Fig. 2B-a), Col(Fig. 2B-b) and the unbiomineralized and biomineralized Col/HA composite scaffold (Fig. 2B-c, d). The FTIR spectrum of the scaffold biomineralized for 6 h showed reduced characteristic peaks of Col at 1637 cm^{-1}, 1241 cm^{-1} and 1528 cm^{-1} (Fig.2B-c, d). The FTIR spectra changes corresponding to 1241 cm^{-1} and 1528 cm^{-1} of the unbiomineralized and biomineralized scaffold were magnified (as shown in the yellow circles of Fig. 2B). This indicated the formation of chemical bonds between the mineralization products on the surface of the nanofibers and amide I, II, and III of Col in the scaffold.

3.3. Mechanism of biomineralization nucleation of the scaffolds

The homogenous deposition of the mineralization product nHA at all structural levels was essential to ensure the mechan-

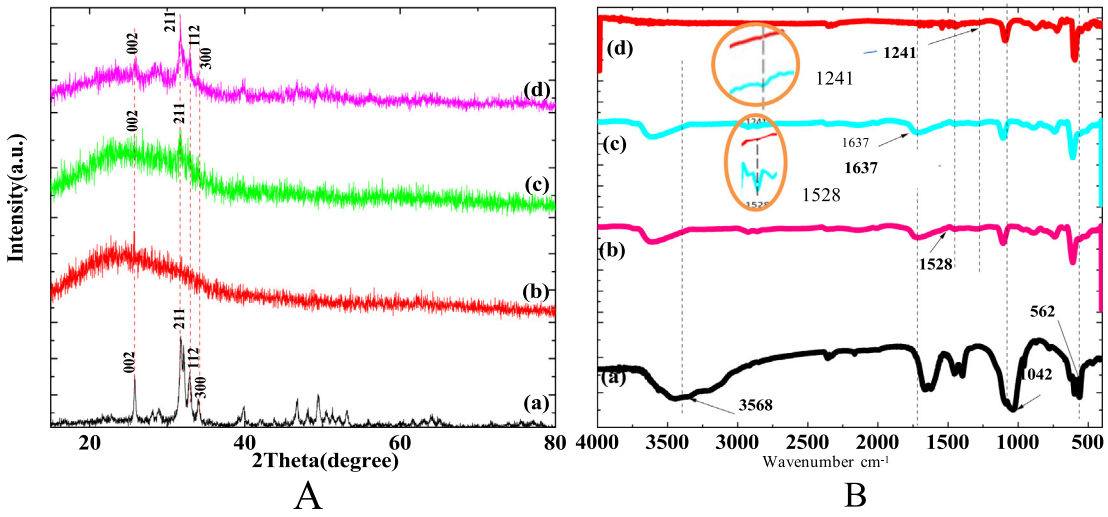

Fig. 2 XRD and FITR profile of Col/HA composite scaffold biomineralized for 6 h (a- HA powder; b- Col; c- Col/HA; d-Col/HA composite scaffold biomineralization for 6 h).

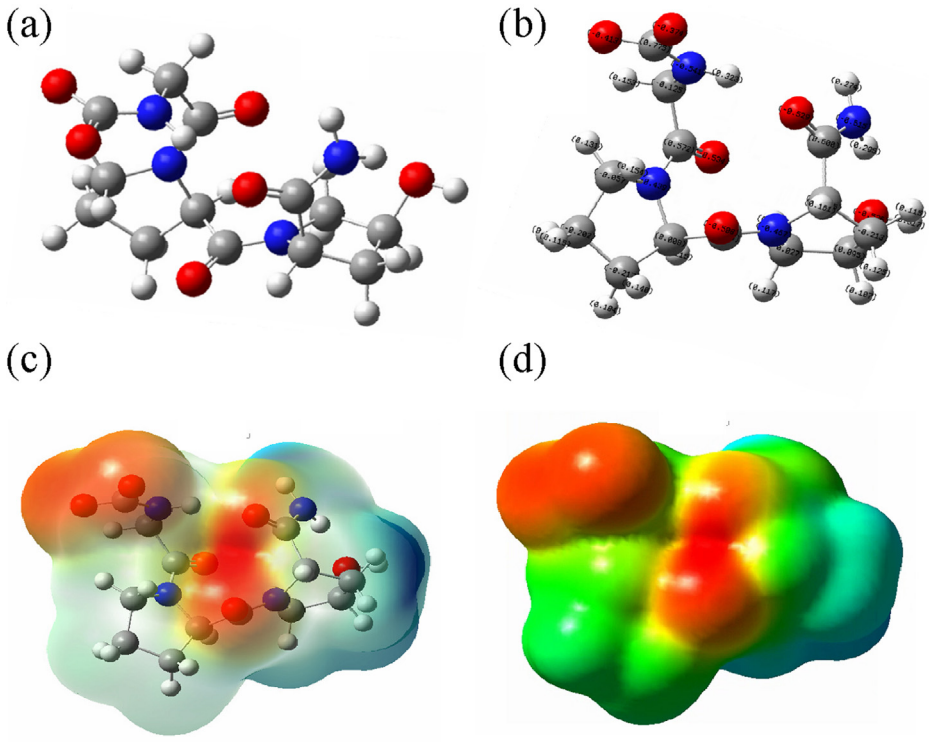

Fig. 3 Simplified Model of Col (a- Optimized atomic structure diagram; b- Atomic charge structure diagram; c- Electron cloud distribution perspective; d- Electrostatic potential diagram).

ical properties of the scaffolds. The manner of nHA binding to the scaffold is also a crucial determinant of the performance of the material. We analyzed the growth pattern of homogeneously deposited nHA array in the scaffold, examined the specific binding location, the mode of binding and the binding energy based on first-principles simulation and calculation.

3.3.1. Col model

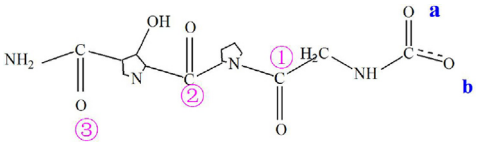

(M)

The unique $(gly\text{-}x\text{-}y)_n$ amino acid sequence pattern and triple helix structure confer unique capabilities on Col as the template for biomineralization (Deymier et al., 2017). Based on the macromolecular structure characteristics of Col and the current computational capacity we constructed a simplified $(gly\text{-}x\text{-}y)_n$ amino acid sequence model of Col, shown as the chemical structure formula M, in which the positions of carboxyl oxygen and carbonyl oxygen were marked for convenience of description.

The atomic geometric structure of model M was shown in Fig. 3a. Fig. 3b-d show the charges that each atom carries in the atomic structure, the electron cloud distribution, and the electrostatic potential diagram. The electronegativity of one oxygen atom in the carboxyl group was about −0.4e, −0.3e for another oxygen atom, and −0.5e for the oxygen in the carbonyl group (Fig. 3b). Both the carboxylic oxygen and carbonyl oxygen can adsorb calcium cationic ions in solution by Coulomb gravity. Fig. 3c shows electron cloud distribution in the atomic structure and the distribution of positive and negative charges around it. In Fig. 3d, the red color represents the negative electrostatic potential, and the blue color represents the positive electrostatic potential. The electron-rich domain is exposed in the optimized structure of carbonyl oxygen and carboxyl oxygen, shown by an intense red color. This structure allows for easy absorption of calcium ions for nucleation.

3.3.2. Combined structure and binding energy of M and Ca^{2+}

To calculate the binding energy between M and Ca^{2+}, we used the general reaction formula and the binding energy formula:

$$2M^{-} + Ca^{2+} = M - Ca - M \quad (1)$$

The reaction structures were modeled using the DFT and the base group B3LYP/6-31G*. The results of analogous computation for the combined structures and the binding energies were presented in Table 1, based on which the binding positions were divided into 3 groups: the carbonyl group, carboxyl group, carbonyl-carboxyl group. The binding energies decreased in the order of carbonyl-carboxyl group, carbonyl group and carboxyl group. The binding strength of various configurations, from weak to strong, was (S8, **S7**) < **S1** < (S10, S2, S9) < (S3, S6, S5, **S4**). We analyzed the simulation results of the nucleation sites in the Col model, and assessed the capacity of the Ca^{2+} bound structure to further bind phosphate and hydroxyl groups to promote HA nucleation. Based on the base group of B3LYP/6-31G* calculation, we optimized the structures of the groups with the lowest binding energy (S4,

S7 and S1), and generated the electron cloud distribution perspective and electrostatic potential diagram of their atomic structure to elucidate the mechanism of mineralization nucleation in the scaffold.

3.3.3. Optimized atomic geometry, electron cloud distribution and electrostatic potential diagram with the lowest binding energy in the 3 groups

The interaction between M and Ca^{2+} was expressed as the general formula M-Ca-M, which represented the individual reactions of the carboxy group, carbonyl group, and carboxyl-carbonyl group with Ca^{2+}, referred to as S1, S7 and S4 reactions in subsequent text, respectively. The general formulas for the 3 reactions were *MCaM-S1* (carboxyl group), *MCaM-S7* (carbonyl group) and *MCaM-S4* (carbonyl-carboxyl group).

S1 reaction: MCaM-S1 (carboxyl group)

In the Col model, the binding energy of Ca^{2+} and carboxyl group in S1 reaction was calculated using the following formula:

$$\Delta E_1 = E(M_1 - Ca - M_1) - E(Ca^{2+}) - 2E(M_1) = -1.01101\ Hartree = -2654.37\ KJ/mol \quad (2)$$

where M_1 represented the two oxygens a and b on the carboxyl group in the Col model, as marked in the atomic structure formula (3) of the reaction.

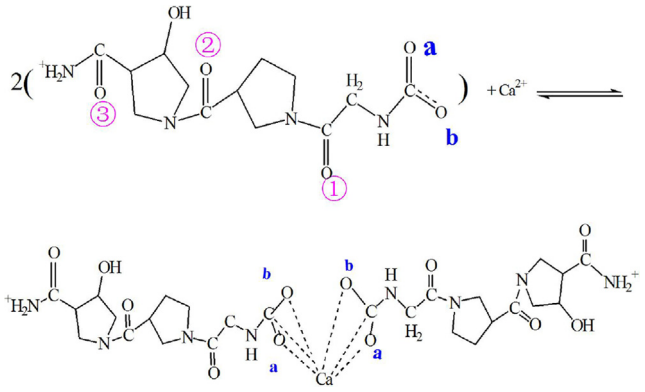

(3)

Fig. 4 showed the optimized atomic geometric structure diagram, the electron cloud distribution perspective and electrostatic potential diagram of the reaction product of carboxyl group in the Col model and Ca^{2+}. As seen in the chemical structure of the reaction product in formula (3) and Fig. 4a, C=O double bond in the carboxyl group opens, and Ca^{2+} bound to oxygen atoms in the two pairs of carboxyl groups in Col. The carbon atoms of the carboxyl group in Col also bound to Ca^{2+}, exerting a force on the C-N bond. Fig. 4b shows the electronegativity of each atom in the structure and the distribution of the surrounding charges. After Ca^{2+} binding with oxygen of the carboxyl group, the surrounding charge is positive (shown by enhanced blue area in Fig. 4b, c). Theoretically, this structure has the ability to further adsorb the negatively charged phosphate and hydroxyl functional groups to form HA nuclei. In addition, the exposed carbonyl and hydroxyl groups (red domains) may also adsorb Ca^{2+} in the solution by Coulomb force to promote HA nucleation.

S7 reaction: MCaM-S7 (carbonyl group)

In S7 reaction, Ca^{2+} binds to carbonyl of the Col model, and the binding energy can be calculated using the formula (4):

$$\Delta E_2 = E(M_2 - Ca - M_2) - E(Ca^{2+}) - 2E(M_2) = -1.03298\ Hartree = -2712.06\ KJ/mol \quad (4)$$

where M_2 represented the oxygen atoms on the tri-pair carbonyl group in the Col model, designated as 1, 2, 3 according to their distance (from near to far) to the carbonyl group, as shown in the formula (5).

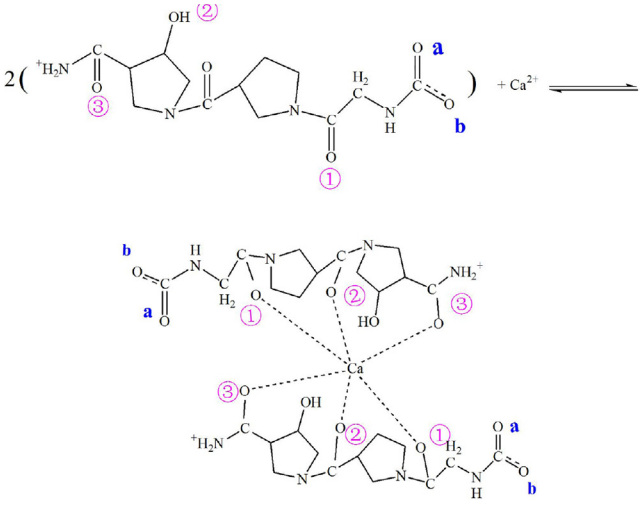

(5)

The reaction equation (5) and optimized atomic geometric chart of the reaction product (Fig. 5a) show that the double bond of the 3 pairs of carbonyl groups is open in the Col model. The 3 pairs of oxygen in the carbonyl group bind to Ca^{2+}, and oxygen in the carbonyl is negatively charged (Fig. 5b) while carbon of the carbonyl is positively charged. The interaction between Ca^{2+} and oxygen of the carbonyl group affects the adjacent C-N bonds. Analysis of electrostatic potentials (Fig. 5c) shows that the red color region of oxygen of the carbonyl group bonding with Ca^{2+} is weakened, and the blue color is not intensified, indicating that in the binding position, the positively charged Ca^{2+} also adsorbs PO_4^{3-} and OH^- groups by Coulomb force and combines with them. The enhanced and exposed red color region in the electrostatic potential diagram corresponds to the distribution of the negative charges of the two oxygens in the carboxyl group and in hydroxyl (Fig. 5b). The central region of the negative charges facilitates the adsorption and binding of Ca^{2+} in the initial stage of scaffold mineralization to promote HA nucleation.

S4 reaction: MCaM-S4 (carbonyl-carboxyl group)

S4 reaction reveals the binding energy of the carboxyl-carbonyl group in Col with Ca^{2+}, calculated using formula (6):

$$\Delta E3 = E(M1 - Ca - M2) - E(Ca2+) - E(M1) - E(M2) = -1.05354\ \ Hartree = -2766.04\ KJ/mol \quad (6)$$

where M_1 and M_2 represent the corresponding oxygen of carboxyl - carbonyl group, respectively. According to the distance to the carboxyl group (from near to far), the oxygens of carbonyl-carboxyl group were designated as a, b and 2; a, b and 3, and are marked in the formula (7).

Table 1 Different configurations and their binding energies of Col and Ca^{2+}.

Structure	Energy(6-31G*)	Energy(6-31G**)	△E	Configuration
Ca^{2+}	−676.866860729	−676.866860729	–	
M-	−1177.15774231	−1177.19416703	–	
MCaM-S1	**−3032.19335307**	**−3032.26603102**	**−1.010836**	**ab-a′b′**
MCaM-S2	−3032.21532638	−3032.28732222	−1.032127	a1-a′1′
MCaM-S3	−3032.23588671	−3032.30873827	−1.053543	ab23-a′b′
MCaM-S4		**−3032.33042246**	**−1.075228**	**ab2-a′b′3′**
MCaM-S5		−3032.32302004	−1.067825	ab2-a′b′3′
MCaM-S6		−3032.32256225	−1.067367	ab23-a′b′3′
MCaM-S7		**−3032.25403859**	**−0.998844**	**123-1′2′3′**
MCaM-S8		−3032.25282425	−0.997629	123-1′2′3′
MCaM-S9		−3032.30825601	−1.053061	a123-1′2′3′
MCaM-S10		−3032.28713815	−1.031943	a123-1′2′3′

* The two oxygens of the carboxyl group were designated as a and b, and the three oxygens of carbonyl groups from near to far from the carboxyl group as 1, 2, and 3.

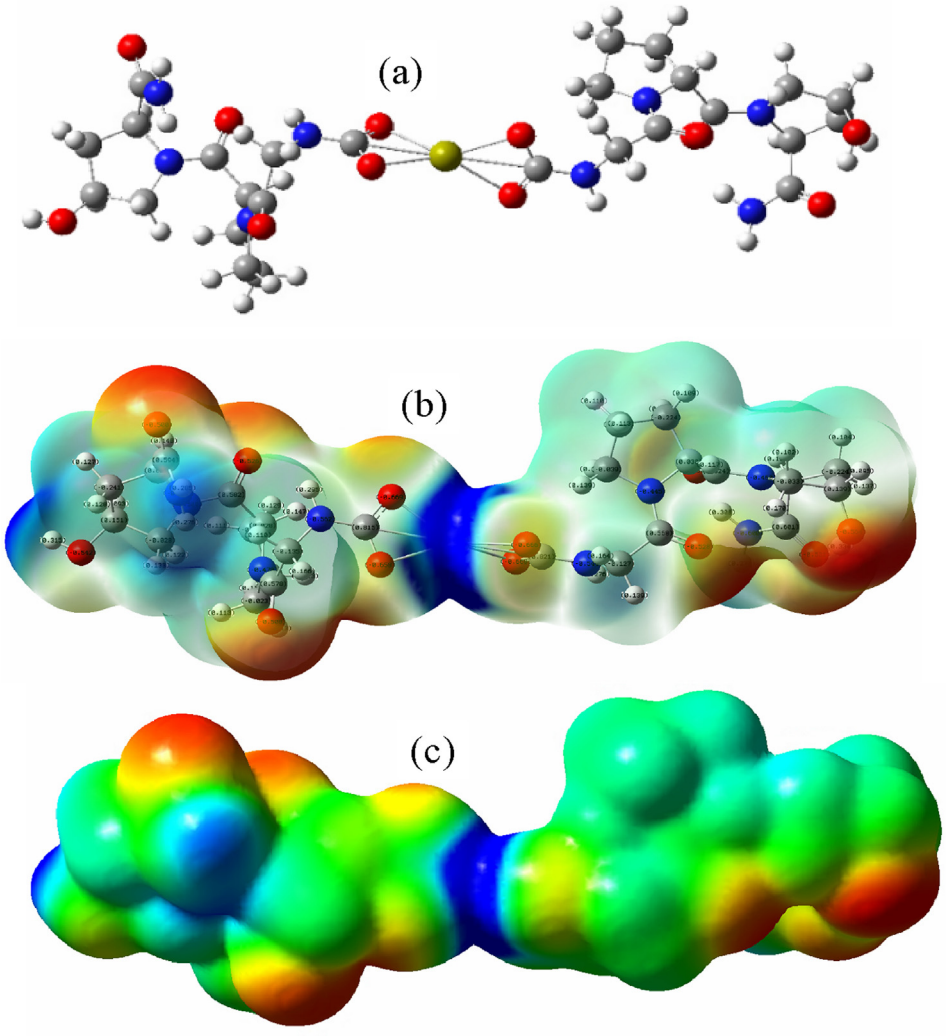

Fig. 4 The model of carboxyl group binding to Ca^{2+} (a- Atomic geometric structure diagram; b- Atomic structure electron cloud distribution perspective; c-Electrostatic potential diagram).

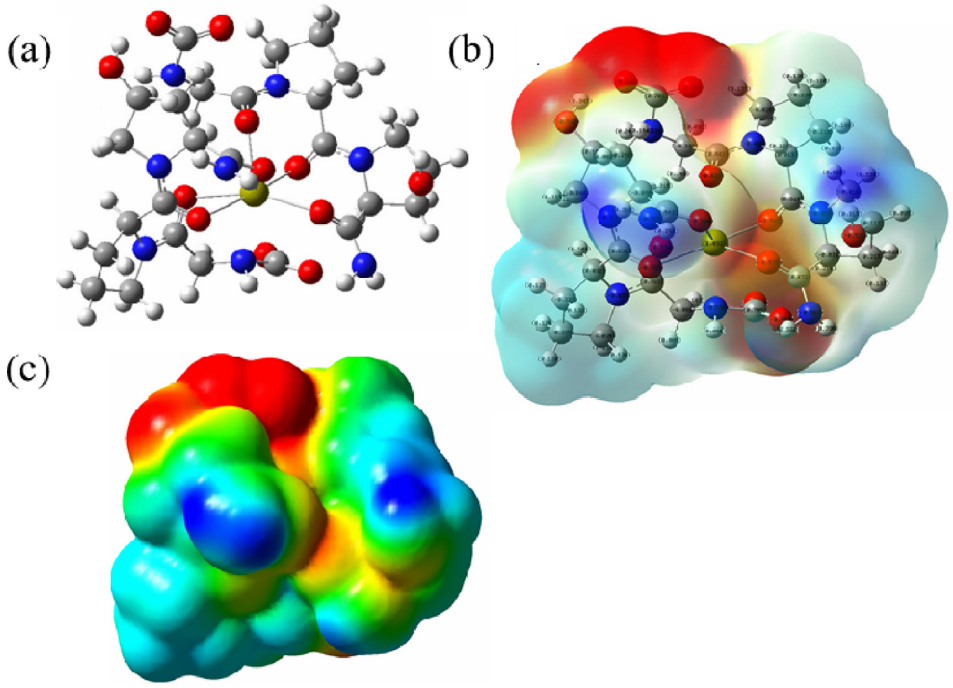

Fig. 5 The model of carbonyl group binding to Ca^{2+} (a- Optimized atomic geometric structure; b- Charge distribution perspective; c- electrostatic potential diagram).

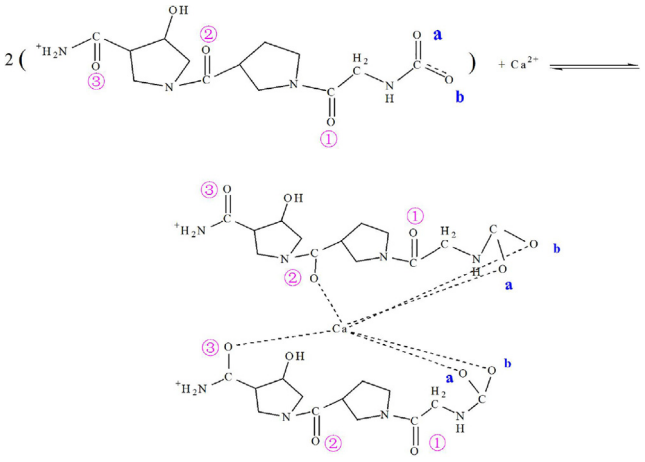

(7)

Based on the optimized atomic geometric structure (Fig. 6a) and the chemical structure of the reaction product, the binding energy is the lowest when Ca^{2+} binds with the 4 oxygen atoms in one pair of carboxyl groups and the 2 oxygen atoms in one pair of carbonyl groups. Before the binding, C=O double bond in carboxyl-carbonyl groups opens. The electron cloud and electrostatic potential are shown in Fig. 6b, c. The red color in the middle region in the electrostatic potential diagram remains intense, demonstrating a negative charge in the region, which is exposed to allow absorption of positively charged ions from the solution by Coulomb forces; but nucleation does not occur in this region as no binding position is available.

The results of simulation showed that the binding energy of the carboxyl-carbonyl group was the lowest, followed by the carbonyl group, and finally the carboxyl group. We optimized the combination of Ca^{2+} and the 3 functional groups of the Col model by the lowest binding energies, and analyzed the optimal atomic geometric structure and the electrostatic potentials corresponding to their lowest binding energies. S1 reaction of the carboxyl group was found to most likely bind Ca^{2+} and promote HA nucleation, and the interatomic action occurred between the 4 oxygen atoms of the carboxyl group at the end of every two groups of amino acids and Ca^{2+} during HA nucleation. The binding energy of S7 reaction in carbonyl group was the lowest to allow nHA nucleation. Although the binding energy of carbonyl-carboxyl group was the lowest in three groups, its electrostatic potential graph showed a strong negative potential after Ca^{2+} binding, and there was no position for cationic binding, thus making nucleation impossible.

These results demonstrate that the oxygen of both carboxyl and carbonyl in Col have negative charges, and the electrostatic potential at this position was also negative, thus the biomineralization at these sites can be improved, as was consistent with the report of Türk et al (Türk et al., 2018).

The homogenous *in situ* deposition of nHA at all structural levels of the scaffold was attributed to the regular distribution of the carboxyl and carbonyl functional groups in the Col component.

3.4. Crystal growth mechanism of nHA array

The nanoscale plate morphology of bone minerals is the basis of bone mechanics and physiology (Persikov et al., 2005), but the mechanisms that regulate nanocrystalline morphology of these minerals remain unclear. To understand the nature of the mechanical properties of the mineralized scaffold, we

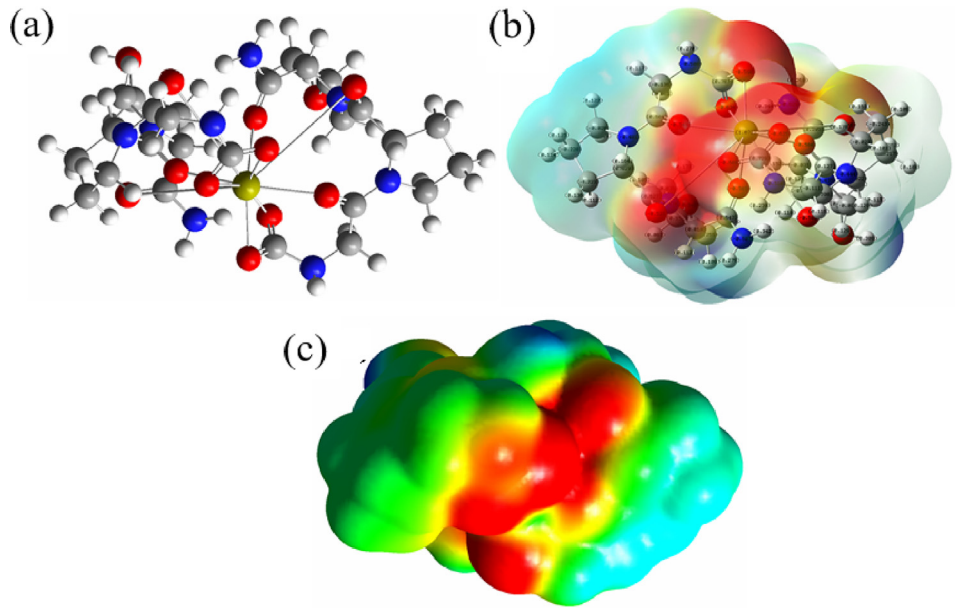

Fig. 6 The model of the mixture of carboxyl and carbonyl groups with Ca^{2+} binding Optimized atomic geometric structure diagram; b- atomic charge distribution perspective; c- electrostatic potential diagram).

explored the crystal growth mechanism of nHA array at different structural levels of the scaffold (Fig. 7). Col protein has a regular triple helix structure consisting of a sequence of regularly distributed amino acids (-gly-pro-hyp-) (Persikov et al., 2005; Yang et al., 2016). Ca^{2+} first binds to a carboxyl or a carbonyl functional group in the Col component of the scaffold, and nucleation is initiated with subsequent binding of PO_4^{3-} and OH^- in the solution till the critical nucleation size is reached. In the solution system, the change of Gibbs free energy of the supersaturated ions during transition from a supersaturated state to an equilibrium state is the driving force for HA nucleation and growth (Kwon et al., 2009). In terms of energy, HA (100) facet is the most hydrophilic (Zhao et al., 2014) and therefore grows preferentially by binding with the hydrated ions in the solution. This is consistent with the previous findings that the crystal facets grow in the order of (100) > (110) > (001) during HA synthesis (Lin et al., 2017); Thus the growth of (100) facet is promoted, while (001) facet is inhibited, resulting in the formation of hexagonal laminar HA crystal that grows along the C axis.

Due to three-strand helical structure of Col and the regular distribution of the functional groups in the amino acids of Col molecules, HA crystals grow continuously in a lamellar form following HA nucleation. To further illustrate the mechanism of HA growth, we expanded the space between the interhelical functional groups of a Col molecule for better visualization of the lamellar HA crystals that grow separately (Fig. 7). In fact, the three-stranded helices are tightly bound, and only the exterior lamellar HA crystals on the three-strand helices can be observed, presenting with a regular flower-like morphology formed by HA binding with the regularly distributed of functional groups.

During nucleation, the binding of Ca^{2+} to the peptide bond oxygen appears to induce significant reconstruction of the polypeptide skeleton from the β-folded sheet to the α-helix and α-helix loops (Zhang et al., 2011). This conformational change is accompanied by the binding of a large number of hydrogen-driven peptides to PO_4^{3-} and OH^- groups of HA, while many -C = O and H-N-group peptide bonds are liberated from the interchain hydrogen bonds, react with Ca^{2+}, and then strongly bind to HA surface. In addition, an increasing number Col nucleation sites are gradually exposed to promote the nucleation and growth of HA, resulting in the generation of HA lamellar-petals of different sizes. With the extension of reaction time, HA grows steadily, but as the space between the three-stranded helices is limited, the separated fractal structure tends to self-assemble, through the hydrogen bond to minimize the surface energy (Liliana et al., 2014), into a more complex flower ball. Fig. 7 shows the simple self-assembly of HA between two strands of the helix, and the formation of a multi-layered nHA flower ball. It can be inferred that if the lamellar nHA are inter-assembled in the space between the 3 strands of the helix, the lamellar structure of the assembled HA flower ball will be more complex. Therefore, nHA array is generated at the regularly distributed nucleation sites with regular self-assembled flower spherical growth under the control of Col template at constant conditions (space and ion concentrations).

3.5. Mechanical properties and a double multilevel mechanical strengthening mechanism of the scaffold

Fig.8 shows the characterization of the mechanical properties of the non-bionic and bionic bone structure scaffolds and the bionic mineralized scaffold, the force and displacement curves of bionic scaffold before and after biomineralization, and the mechanism of multi-level mechanical strengthening of the scaffold. Comparison of the mechanical properties of non-bionic and the biomimetic scaffolds, it showed that the latter had a 1.47-fold greater compression strength and a nearly 5-fold greater elastic modulus than the former, indicating that the

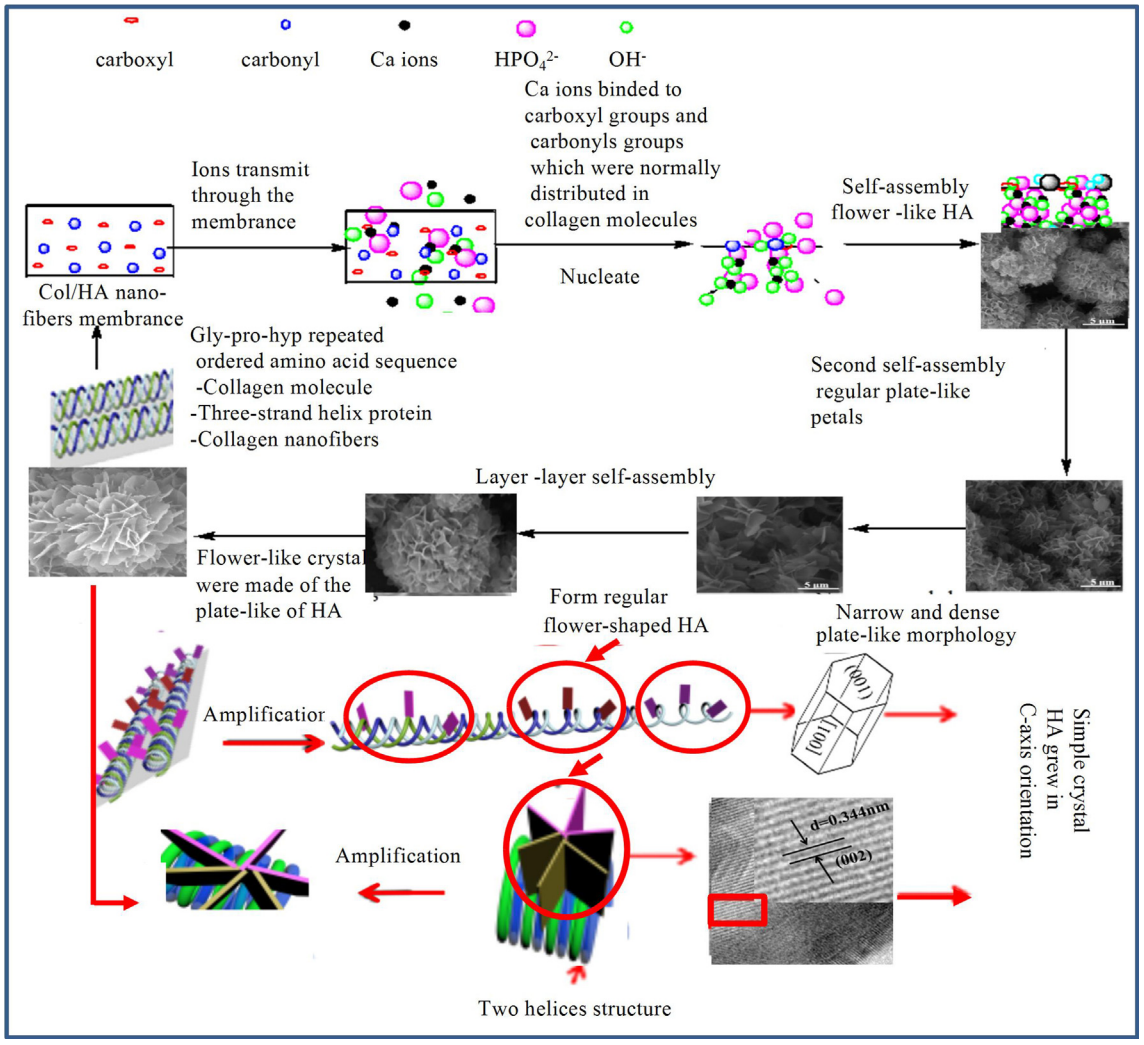

Fig. 7 Crystal growth mechanism of nHA array.

multi-scale biomimetic structure allows the scaffold to have excellent mechanical properties (Fig. 8A). After mineralization, the bionic Haversian scaffold had an enhanced compressive strength and Young's modulus increased by 9.7 and 1.4 folds after mineralization, respectively.

Natural compact bones had an axial compressive strength of 131–224 MPa and a Young modulus of 17–20 GPa (Shin et al., 2015), showing an superior compressive property to that of the bionic bone scaffold. But the compressive stress of the bionic bone scaffold was much higher than that of non-biomimetic bone scaffolds the study, other composite Col-based scaffolds (Shirin et al., 2019; Türk et al., 2018; Shirin et al., 2016; Sara et al., 2010; Hassani et al., 2022; Zhou et al., 2014), simple biomimetic bone scaffolds with a hierarchical structure (Türk et al., 2018; Taylor et al., 2017; Liu et al., 2021); a bionic scaffold with bone fibers arranged at different angles (Zhao and Liang, 2017) and biomimetic scaffolds with a honeycomb structure (Wu et al., 2014). As a Haversian microstructure results from the adaptation for high compressive strength (Black et al., 1974), a more sophisticated bionic Haversian microstructure should be a solution for improving the mechanical property of the scaffold material. The bionic microstructure and the Haversian microstructure of natural bone tissue differ in that the size of the Haversian motifs of the latter is not uniform, ranging from 100 μm to 500 μm (Toader et al., 2017), whereas the motif size of the synthesized scaffold is roughly uniform (∼500 μm). In natural bone tissues, the Col fibers are aligned in parallel along the longitudinal axis or transverse to the longitudinal axis in the motifs (Wu and Zheng, 1999), but the motifs of the synthesized scaffold in this study contained only Col fibers parallel to the longitudinal axis. These two differences may explain the inferior mechanical properties of the scaffold in comparison with the natural bone tissues. In the future work, modifications of the motif size and Col fiber alignment in the scaffold should be tested to improve the mechanical properties of the scaffold. More sophisticated bionic components and Haversian microstructure will also be used to better mimic the composition and structures of natural bone tissues. The compression performance curves of the biomimetic scaffold before and after mineralization show consistent compression characteristics between the scaffold and HM type sea urchin spine (Toader et al., 2017) (Fig. 8).

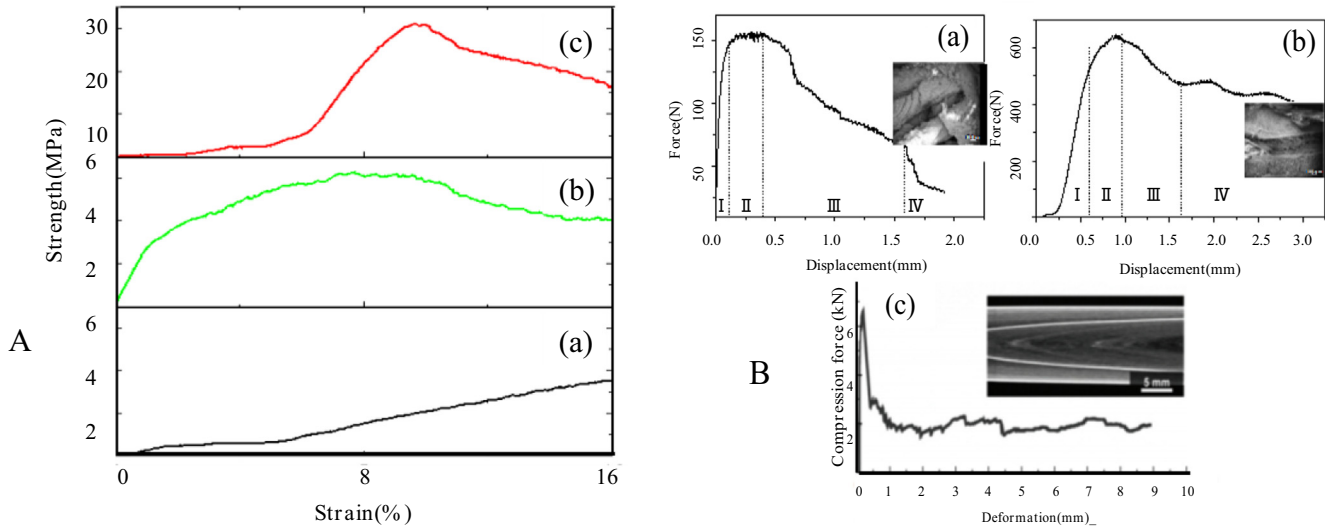

Fig. 8 The stress-strain curve and Force and displacement curve of the scaffolds (A- (a- Non-bionic bone structure scaffold, b- Bionic bone structure scaffold, c- The bionic mineralized structure scaffold), B- Force and displacement curve (a- Before biomineralization, b- After biomineralization, c- HM of the sea urchin(Toader et al., 2017)).

SEM observation of compression failure of the scaffolds before mineralization revealed clear separation of the motifs and fibers in the membrane along the long axis (Fig. 8B-a), as compared with discontinuous fracture of the fiber membrane in the mineralized scaffold (Fig. 8B-b) due to increased interfibrous and interlaminar bonding strength after mineralization.

The mechanical performance of composite scaffold is closely related with the reinforcing substrate interface, the two phases of reinforcing ties and bridges connected to the matrix, the interface microstructure and the combination property. The multi-scale structure of the scaffold forms a multi-level interface with *in situ* deposition nHA at the interfaces at all levels. Mineralization causes nHA to interlock with the Col triple helix to generate reinforcement. Wu and Zheng (1999) reported an ideal *in situ* matching between the *in-situ* generated second phase and the matrix, which significantly improved the bonding of the two-phase interface in the composite material, and at the same time avoided potential uneven dispersion of the second phase and weak interface bonding in the conventional approach of material preparation.

We investigated the mechanism of mechanical strengthening of bionic bone structure Col/HA composite scaffold at compression direction along the long axis of the nanofibers (Fig. 9). The first structural level of the scaffold was the nano-scale fibers and nHA reinforcement. In the unmineralized scaffold, nHA framework fiber impregnating Col forms composite fibers and nHA forms composite reinforcement within the fibers. In the mineralization process of the scaffold, nHA deposited on porous membrane, and evenly distributed on the nanofibers (Fig. 1c-f). The *in situ* deposited nHA and the carboxyl or/and carbonyl functional groups in Col components of the fibers form bonds that anchor nHA on the fiber surface, which also reduces the defect of nanoparticle agglomeration. The very large surface area of HA nanoparticles facilitates the full contact of nHA with the nanofibers and strengthens their bonding (Fig. 9) to improve the strength of the nanofibers. The numerous Col/HA composite nanofibers in the scaffold are interlaced with each other, and the nanoparticles and the fibers are bound together as two continuous phases to produce a strengthening effect. The secondary strengthening of the nanofibers and the increase in the bonding strength between the nanofibers significantly enhances the mechanical properties of the scaffolds.

The next structural level of the scaffold is the micron scale bionic bone motifs, assembled by the fiber membrane coiling layer upon layer. The nanofibers that assemble the motifs are aligned in parallel along the long axis to mimic a bone multilayer structure, so that the strength can be greatly improved in the vertical direction to the long axis. After mineralization, a large quantity of newly generated nHA bonding with the fiber membrane enhances the chemical bonding to strengthen the interface. In addition, the fibrous membrane layers are cross-linked due to *in situ* nHA deposition on the membrane surface, which further enhances the bonding between the membrane layers (Fig. 8B-b) and increases the deformation resistance of a single bionic bone motif, resulting in enhanced mechanical properties of the scaffold.

At the macroscopic level (millimeter-sized) of the scaffold, the combination of the biomimetic bone motifs contributes to mechanical strengthening of the construct. The biomimetic bone motifs are orderly arranged in parallel with the long axis of the fibers, and are combined with one another by Col, which significantly improves the deformation resistance in the vertical direction to the long axis of the fibers. The interfacial gaps among the motifs allow the motifs to access the mineralization solution to form nHA deposition at the interface. The mineralization product nHA forms a strong interface binding with the motifs and results also in a strong bonding between the adjacent mineralized bone motifs to improve the mechanical properties of the scaffold.

To summarize, the mechanical properties of this bionic scaffold are enahnced not only by its multi-scale structure, the presence of nHA in the nanofibers, Col bonding between the membrane layers and among the bionic bone motifs, but also by the mineralization product nHA homogeneously

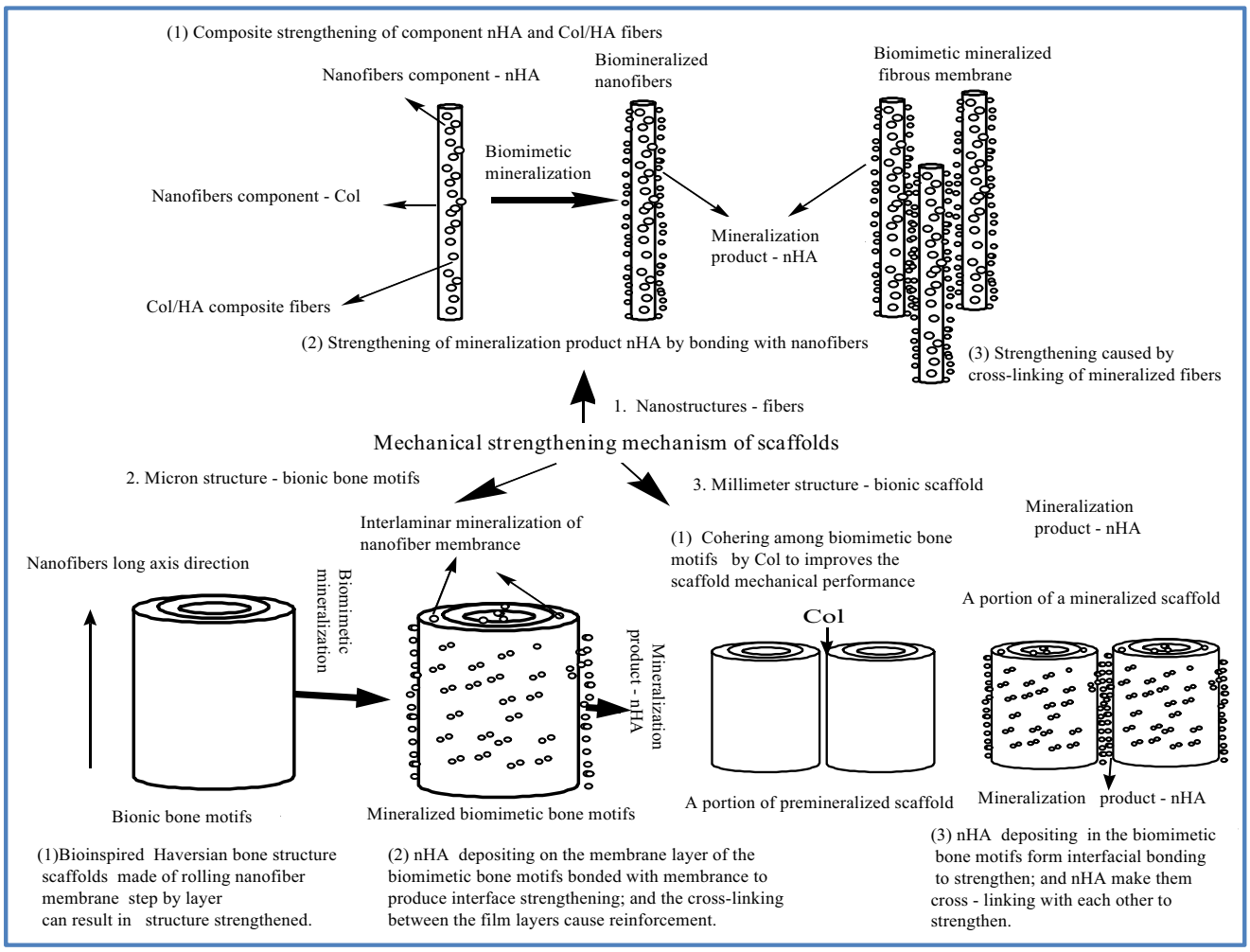

Fig. 9 The double multistage strengthening mechanism of the scaffolds.

deposited at all the structural levels of the scaffold. In addition, the interface strengthening by massive chemical bonding, which is the mechanism for secondary strengthening, further enhances deformation resistance and improves the mechanical properties of the scaffold.

4. Conclusions

We constructed a biomineralized biomimetic bone scaffold that contained biomimetic bone components with multi-scale structures (from nanofibers to micron bionic bone motifs and to bionc bone scaffold) and excellent compression properties. The multi-scale bionic bone structure and biomimetic mineralization of the Col/nHA nanofiber-based scaffold, allows double reinforcement of its mechanical properties, and can be potentially used for repairing bone tissue defects. Our results shed light on a new strategy for synthesis of biomimetic functional materials for bone tissue regeneration.

Acknowledgement

This work was supported by Natural Science Foundation of China (No. 51372199), Basic Research Project of Science and Technology Strategic Cooperation between Luzhou Municipal People's Government and Southwest Medical University (20YKDYYJC0130), Science and Technology Achievement Transformation Project of Southwest Medical University (No.00031483) and Doctoral Research Initiation Fund of Affiliated Hospital of Southwest Medical University (No.20084).

References

Bian, T.R., Zhao, K., Meng, Q.N., et al, 2019. The construction and performance of multi-level hierarchical hydroxyapatite (HA)/Col composite implant based on biomimetic bone Haversian motif. Mater. Des. 162, 60–69.

Black, J., Mattson, R., Korostoff, E., 1974. Haversian osteons: Size, distribution, internal structure, and orientation. J. Biomed. Mater. Res. 8, 299–319.

Chen, X.X., Zhu, L., Wen, W., et al, 2019. Biomimetic mineralisation of eggshell membrane featuring natural nanofiber network structure for improving its osteogenic activity. Colloid Surf. B 179, 299–308.

Cheng, C.W., Solorio, L.D., Alsberg, E., 2014. Decellularized tissue and cell-derived extracellular matrices as scaffolds for orthopaedic tissue engineering. Biotechnol. Adv. 32 (2), 462–484.

Cui, F.Z., Wang, X.M., Li, H.D., 2009. Assembly mechanism of mineralized Col. Mater China 28 (4), 34–39.

Deng, Y., Sun, Y., Bai, Y., et al, 2016. In Vitro Biocompability/osteogenesis and in vivo bone formation evalution of peptide-decorated apatite nanocomposites assisted via polydopamine. J. Biomed. Nanotechnol. 12, 602–618.

Deymier, A.C., Nair, A.K., Depalle, B., et al, 2017. Protein-free formation of bone-like apatite: New insights into the key role of carbonation. Biomaterials 127, 75–88.

Dieguez, O., Tinte, S., Antons, A., et al, 2004. Abinitio study of the phase diagram of epitaxial BaTiO3. Phys. Rev. B 69, 212101–212104.

Dieguez, O., Rabe, K.M., Vanderbilt, D., 2005. First-principles study of epitaxial strain in perovskites. Phys. Rev. B 72, 144101–144109.

Dorozhkin, S., 2009. Calcium orthophosphate-based biocomposites and hybrid biomaterials. J. Mater. Sci. 44, 2343–2387.

Fatemeh, M., Hossein, H., Mohammad, A.S., et al, 2015. Silk as a potential candidate for bone tissue engineering. J. Control. Release 215, 112–128.

Gkioni, K., Leeuwenburgh, S.C.G., Douglas, T.E.L., et al, 2010. Mineralization of hydrogels for bone regeneration. Tissue Eng. Part B - Rev. 16, 577–585.

Guo, X.D., Du, J.Y., Zheng, Q.X., et al, 2002. Molecular tissue engineering:concepts, status and challenges. J WUHAN University Technol., Mater. Sci. Ed. 17 (3), 30–34.

Guo, X.D., Zheng, Q.X., 2004. Research progress in repairing bone defect with tissue engineering technology. Foreign Med. Biomed. Eng. Sect. 27 (5), 270–273.

Hassani, A., Khoshfetrat, A.B., Rahbarghazi, R., et al, 2022. Col and nano-hydroxyapatite interactions in alginate-based microcapsule provide an appropriate osteogenic microenvironment for modular bone tissue formation. Carbohyd. Polym. 277, 118807.

He, M.M., Zhang, Y.P., Munyemana, J.C., et al, 2017. Tuning the hierarchical nanostructure of hematite mesocrystals via Col-templated biomineralization. J. Mater. Chem. B 5 (7), 1423–1429.

Huang, C., Zhou, Y., Tang, Z., et al, 2011. Synthesis of multifunctional Fe3O4 core/hydroxyapatite shell nanocomposites by biomineralization. Dalton Trans. 40, 5026–5031.

Hyeryeon, P., Jin, L.D., Lee, S.H., et al, 2016. Nanofibrous mineralized electrospun scaffold as a substrate for bone tissue regeneration. J. Biomed. Nanotechnol. 12, 2076–2082.

Keaveny, T.M., Morgan, E.F., Niebu, G.L., 2001. Biomechanics of trabecular bone. Annu. Rev. Biomed. Eng. 3, 307–333.

Kesireddy, V., Kasper, F.K., 2016. Approaches for building bioactive elements into synthetic scaffolds for bone tissue engineering. J. Mater. Chem. B 4 (42), 6773–6820.

Kwon, K.Y., Wang, E., Chang, N., et al, 2009. Characterization of the Dominant Molecular Step Orientations on Hydroxyapatite (100) Surfaces. Langmuir 25 (13), 7205–7208.

Lai, B., Kornev, I.A., Bellaiche, L., Salamo, G.J., 2005. Phase diagrams of epitaxial BaTiO3 ultrathin films from first principles. Appl. Phys. Lett. 86, 132904–132906.

Lakshmi, S.N., Cato, T.L., 2006. Polymers as biomaterials for tissue engineering and controlled drug delivery. Adv. Biochem. Eng. Biotechnol. 102, 47–90.

Lee, H.S., Mizoguchi, T., Yamamoto, T., Kang, S.J.L., Ikuhara, Y., 2007. First-principles calculation of defect energetics in cubic-BaTiO3 and a comparison with SrTiO3. Acta Mater. 55, 6535–6540.

Li, Y.P., Jose, C.R.C., Aparicio, C., 2017. Intrafibrillar mineralization of self-Assembled elastin-like recombinamer fibrils. Appl. Mater. Inter. 9 (7), 5838–5846.

Lievers, W.B., Petryshyn, A.C., Poljsak, A.S., 2010. Specimen diameter and "side artifacts" in cancellous bone evaluated using end-constrained elastic tension. Bone 47, 371–377.

Lievers, W.B., Waldman, S.D., Pilkey, A.K., 2010. Minimizing specimen length in elastic testing of end-constrained cancellous bone. J. Mech. Behav. Biomed. Mater. 3, 22–30.

Liliana, P.C., Magda, L.E., Jaime, E.R.V., 2014. Scaffold design for bone regeneration. J. Nanosci. Nanotechnol. 14 (1), 15–56.

Lin, Z.Y., Hu, R., Zhou, J.Z., 2017. A further insight into the adsorption mechanism of protein on hydroxyapatite by FTIR-ATR spectrometry. Spectrochim. Acta A 172, 527–531.

Liu, H., Qiu, L., Liu, H., et al, 2021. Effects of Fiber Cross-Angle Structures on the Mechanical Property of 3D Printed Scaffolds and Performance of Seeded MC3T3-E1 Cells. ACS Omega 6, 33665–33675.

Mao, L.B., Gao, H.L., Yao, H.B., et al, 2016. Synthetic nacre by predesigned matrix-directed mineralization. Science 354, 107–110.

Matsunaga, K., 2008. First-principles study of substitutional magnesium and zinc in hydroxyapatite and octacalcium phosphate. J. Chem. Phys. 128 (24), 24510101–24510110.

Mayya, A., Banerjee, A., Rajesh, R., 2016. Haversian microstructure in bovine femoral cortices: An adaptation for improved compressive strength. Mater. Sci. Eng., C 59, 454–463.

Mehdi, F., Fatemeh, M., Mohammad, A.S., et al, 2016. Importance of dual delivery systems for bone tissue engineering.Journal of Controlled Release. J. Control. Release 225, 152–169.

Meyer, B., Vanderbilt, D., 2001. Abinitio study of BaTiO3 and PbTiO3 surfaces in external electric fields. Phys. Rev. B 63, 205426–205435.

Meyers, M.A., Chen, P.Y., Lin, A.Y.M., et al, 2008. Biological materials: structure and mechanical properties. Prog. Mater Sci. 53 (1), 1–206.

Navarro, M., Michiardi, A., Castano, O., et al, 2008. Biomaterials in orthopaedics. J. R. Soc. Interface 5, 1137–1158.

Norwitz, G., Nataro, N., Keliher, P., 1986. Study of the steam distillation of phenolic compounds using ultraviolent spectrometry. Anal. Chem. 58, 639–640.

Pei, F., Ye, K., Li, Y., et al, 2019. Molybdenum disulfide nanosheets embedded with nanodiamond particles:co-dispersion nanostructures as reinforcements for polymer scaffolds. Appl. Mater. Today 17, 216–226.

Pereira, D.D.M., Habibovic, P., 2018. Biomineralization-inspired material design for bone regeneration. Adv. Healthcare Mater. 7 (22), 1800700–1800718.

Persikov, A.V., Ramshaw, J.A.M., Kirkpatrick, A., et al., 2005. Electrostatic interactions involving lysine make major contributions to col triple-helix stability. Biochem., 44:1414-1422.

Persikov, A.V., Ramshaw, J.A.M., Kirkpatrick, A., et al., 2005. Electrostatic interactions involving lysine make major contributions to col triple-helix stability. Biochemistry, 44, 1414-1422.

Reznikov, N., Steele, J.A.M., Fratzl, P., et al, 2016. A materials science vision of extracellular matrix mineralization. Nat. Rev. Mater. 1 (8), 1–37.

Salgado, C.L., Grenho, L., Fernandes, M.H., et al, 2016. Biodegradation, biocompatibility, and osteoconduction evaluation of Col-nanohydroxyapatite cryogels for bone tissue regeneration. J Biomed. Mater. Res. A. 4 (1), 57–70.

Sara, M., Hossein, H., Nadereh, G.E., et al, 2010. Proliferation and Differentiation of Mesenchymal Stem Cell on Col Sponge Reinforced with Polypropylene/Polyethylene Terephthalate Blend Fibers. Tissue Eng. Pt A 16 (12), 3821–3830.

Scarano, A., Carlo, D., Quaranta, F., et al, 2003. Bone response to zirconia ceramic implants: an experimental study in rabbits. J. Oral Implantol. 29, 8–12.

Seal, B.L., Otero, T.C., Panitch, A., et al, 2001. Polymeric biomaterials for tissue and organ regeneration. Mater. Sci. Eng., R 34, 147–230.

Shin, K.H., Kim, J.W., Koh, Y.H., et al, 2015. A novel self-assembly-induced 3D plotting for macro/nano-porous Col scaffolds comprised of nanofibrous Col filaments. Mater. Lett. 143, 265–268.

Shirin, T., Hojjat, N.M., Fatemeh, K., et al, 2016. PGA-incorporated Col: toward a biodegradable composite scaffold for bone-tissue engineering. J. Biomed. Mater. Res. A 104, 2020–2028.

Shirin, T., Hojjat, N.M., Fatemeh, K., et al, 2019. Bone defect healing is induced by Col sponge/polyglycolic acid. J. Mater. Sci.: Mater. Med. 30, 33.

Shuai, C.J., Li, Y., Wang, G.Y., et al, 2019. Surface modification of nanodiamond: Toward the dispersion of reinforced phase in poly-L-lactic acid scaffolds. Int. J. Biol. Macromol. 126, 1116–1124.

Shuai, C.J., Yang, W.J., Feng, P., et al, 2021. Accelerated degradation of HAP/PLLA bone scaffold by PGA blending facilitates bioactivity and osteoconductivity. Bioact. Mater. 6, 490–502.

Sigel, H., Martin, R.B., 1982. Coordinating properties of the amide bond. stability and structure of metal ion complexes of peptides and related ligands. Chem. Rev. 82, 385–426.

Smith, L.J., Deymier, A.C., Boyle, J.J., et al, 2015. Tunability of Col matrix mechanical properties via multiple modes of mineralization. Interface Focus 6 (1), 1–15.

Sugandha, C., Anuj, K., Jahir, H.F.S., 2019. Development of biomimetic electrospun polymeric biomaterials for bone tissue engineering. A review. J. Biomater. Sci.-Polym. 30 (14), 1308–1355.

Takahashi, H., Yashima, M., Kakihana, M., et al, 2001. A differential scanning calorimeter study of the monoclinic (P21/b) hexagonal (P63/m) reversible phase transition in hydroxyapatite. Thermochim. Acta 371 (1/2), 53–56.

Tang, S.X., Dong, Z.Y., Ke, X., et al, 2021. Advances in biomineralization-inspired materials for hard tissue repair. Int. J. Oral Sci. 13 (1), 42.

Taylor, B.L., Limaye, A., Yarborough, J., et al, 2017. Investigating processing techniques for bovine gelatin electrospun scaffolds for bone tissue regeneration. Biomaterials 105 (5), 1131–1140.

Toader, S.N., Sobek, W., Nicke, K.G., 2017. Energy absorption in functionally graded concrete bioinspired by sea urchin. J. Bionic Eng. 14, 369–378.

Türk, S., Altınsoy, I., Çelebi Efe, G., et al, 2018. 3D porous Col/functionalized multiwalled carbon nanotube/chitosan/hydroxyapatite composite scaffolds for bone tissue engineering. Mater. Sci. Eng. C 92, 757–768.

Türk, S., Altınsoy, İ., ÇelebiEfe, G., et al, 2018. The effect of reduction of graphene oxide on the formation of hydroxyapatite and tricalcium phosphate. Vacuum 148, 1–10.

Turnbull, G., Clarke, J., Picard, F., et al, 2018. 3D bioactive composite scaffolds for bone tissue engineering. Bioactive Mater. 3, 278–314.

Unnithan, A.R., Arathyram, R.S., Kim, C. S., 2015. In: Thomas, S., Grohens, Y., Ninan, N.B.T.-N.A. for T.E. (Eds.), Chapter 7 - Scaffolds with Antibacterial Properties. William Andrew Publishing, Oxford, pp. 103-123.

Walsh, P.J., Fee, K., Clarke, S.A., et al, 2018. Blueprints for the next generation of bioinspired and biomimetic mineralised composites for bone regeneration. Mar. Drugs 16 (8), 288–310.

Wang, P., Zhao, L., Liu, J., et al, 2014. Bone tissue engineering via nanostructured calcium phosphate biomaterials and stem cells. Bone Res. 3, 139–151.

Wilcock, C.J., Stafford, G.P., Miller, C.A., et al, 2017. Preparation and antibacterial properties of Silver-doped nanoscale hydroxyapatite pastes for bone repair and augmentation. J. Biomed. Nanotechnol. 13, 1168–1176.

Wu, S.L., Liu, X.M., Yeung, K.W.K., Liu, C.S., Yang, X.J., 2014. Biomimetic porous scaffolds for bone tissue engineering. Mater. Sci. Eng., R 80, 1–36.

Wu, J.M., Zheng, S.L., 1999. Particle-reinforced aluminum-basedinstiucomposites. Mater. Rev. 5, 52–54.

Xie, J.J., Ping, H., Tan, T.N., et al, 2019. Bioprocess-inspired fabrication of materials with new structures and functions. Prog. Polym. Sci. 105, 1–49.

Yang, M.Y., Wang, J., Zhu, Y., et al, 2016. Bio-templated growth of bone minerals from modified simulated body fluid on nanofibrous decellularized natural tissues. J. Biomed. Nanotechnol. 12, 753–761.

Yi, S., Ding, F., Gong, L.L., 2017. Extracellular matrix scaffolds for tissue engineering and regenerative medicine. Curr. Stem. Cell. Res. T 12, 233–246.

Yu, Y.J., Ren, S.S., Yao, Y.F., 2017. Electrospun fibrous scaffolds with iron-doped hydroxyapatite exhibit osteogenic potential with static magnetic field exposure. J. Biomed. Nanotechnol. 13, 835–847.

Zhang, Y., Liu, Y., Ji, X.B., 2011. Fabrication of flower-like hydroxyapatite agglomerates with the assistant of bamboo membrane. Mater. Lett. 65, 1982–1985.

Zhang, K., Wang, S.P., Zhou, C.C., 2018. Advanced smart biomaterials and constructs for hard tissue engineering and regeneration. Bone Res. 6 (1), 31–46.

Zhao, H.X., Liang, W.H., 2017. A novel comby scaffold with improved mechanical strength for bone tissue engineering. Mater. Lett. 194, 220–223.

Zhao, W., Xu, Z., Yang, Y., et al, 2014. Surface energetics of the hydroxyapatite nanocrystal–water interface: a molecular dynamics study. Langmuir 30 (44), 13283–13292.

Zheng, Q.X., Guo, X.D., 2003. Advances in bone tissue engineering. Chinese J. Exp. Surg. 20 (6), 487–488.

Zheng, Q.X., Guo, X.D., 2004. Nanobiological medical materials-Nanomedicine, Editor-in-chief xu Huibi. Tsinghua University Press, pp. 267–298.

Zhou, C.C., Ye, X.J., Fan, Y.J., 2014. Biomimetic fabrication of a three-level hierarchical calcium phosphate/Col/hydroxyapatite scaffold for bone tissue engineering. Biofabrication 6, 1–12.

Zhu, L.S., Luo, D., Liu, Y., 2020. Effect of the nano/microscale structure of biomaterial scaffolds on bone regeneration. Int. J. Oral Sci. 12 (1), 41368–41383.

Zimmermann, G., Moghaddam, A., 2011. Allograft bone matrix versus synthetic bone graft substitutes. Injury 42, S16–S21.